Molecular-dynamics simulations of cold single-species and multispecies ion ensembles in a linear Paul trap

C. B. Zhang, D. Offenberg, B. Roth, M. A. Wilson, and S. Schiller
Institut für Experimentalphysik, Heinrich-Heine-Universität Düsseldorf, 40225 Düsseldorf, Germany
(Received 19 April 2007; published 30 July 2007)

The properties of cold ion plasmas with large numbers (>200) of laser- and sympathetically cooled species are modeled in detail using molecular dynamics simulations. We describe how to extract temperatures and ion numbers from CCD images. The identification of the ion species by excitation of their oscillation modes is discussed. The sympathetic cooling efficiency, effects of the rf micromotion and of collision heating by a neutral background gas are analyzed, in part experimentally.

DOI: 10.1103/PhysRevA.76.012719 PACS number(s): 31.15.Qg, 32.80.Pj, 33.80.Ps, 39.25.+k

I. INTRODUCTION

Sympathetic cooling by laser-cooled atomic ions has been established as a powerful method to produce a vast variety of trapped, cold ($\ll 1$ K) atomic and molecular species [1–4]. These samples with temperatures in the order of tens of mK are well suited for studies of chemical reactions [5–8] and spectroscopy, including high-resolution spectroscopy [9,10].

In order to understand and characterize such cold ion plasmas, molecular dynamics (MD) simulations [11,12] are well suited. Simulations can be performed for ion clusters containing several ion species with ion numbers up to several thousand ions. In early studies of one-component (species) plasmas the particle arrangement [13], the ion crystal structure [14], and rf heating [15] were investigated, in order to understand the basic properties of the systems. More recently, simulations have considered ensembles containing dissimilar ion species, for example atomic ions of equal charge but different mass [16] or mixtures of atomic and molecular ions. Simulations include, for example, studies of the ion mass range which can be sympathetically cooled [17], interactions between a few highly charged ions and large numbers of laser-cooled atomic ions [18], and temperature determination of sympathetically cooled heavy singly-charged molecular ions [4]. However, such studies are still few and specialized. There is a foreseeable need for simulations adapted to the particular experimental configuration, in order to understand the interaction of different ion species, time-dependent behavior, and to assist in the interpretation of new observations. Conversely, the simulation models can also be verified and improved by comparing their results with experimental data.

In our experiments with sympathetically cooled ions in linear Paul traps we employ two main methods. The time evolution of the total laser-cooled ions' fluorescence offers a first possibility to analyze the properties of the trapped ion ensembles. A resonant excitation of ion oscillations, for example, leads to changes in the fluorescence and can be used for non-destructive mass measurement of the confined ions [19]. A second method is based on reaching sufficiently low temperatures of the laser cooled ion ensembles when structured ensembles form [20], which can be imaged by a CCD camera. Figure 1 shows a CCD image of a $^9Be^+$ ion crystal (cluster) taken perpendicularly to the trap axis [7]. From the crystal's shape and structure certain basic properties such as ion numbers and temperatures can be deduced by comparison with simulated images.

In this article, we present a simulation model for cold multispecies ion crystals. The implementation of heating effects and laser cooling is discussed in detail. We introduce a method to extract ion numbers and temperatures of laser-cooled and sympathetically cooled ions from CCD images of ion crystals via simulations. The process of sympathetic cooling as well as the effects of rf micromotion are studied. We also simulate aspects of secular excitation of ions for the purpose of species identification.

II. SIMULATION MODEL

A. Equations of motion and forces

Our simulations of multispecies ion crystals in linear Paul traps are based on solving Newton's equations of motion for all laser-cooled and sympathetically cooled ions

$$m_i\ddot{\boldsymbol{r}}_i = \boldsymbol{F}_i(\boldsymbol{r}_1, \ldots \boldsymbol{r}_{N_{\mathrm{LC}}+N_{\mathrm{SC}}}, \boldsymbol{v}_1, \ldots \boldsymbol{v}_{N_{\mathrm{LC}}+N_{\mathrm{SC}}}, t) = \boldsymbol{F}_i^{\mathrm{trap}} + \boldsymbol{F}_i^{\mathrm{Coulomb}} + \boldsymbol{F}_i^{\mathrm{stochastic}} + \boldsymbol{F}_i^{\mathrm{laser}}, \quad (1)$$

where $i=1, \ldots, N_{\mathrm{LC}}+N_{\mathrm{SC}}$ (N_{LC} and N_{SC} are the numbers of laser-cooled and sympathetically cooled ions, respectively). Masses, positions and velocities are m_i, $\boldsymbol{r}_i$, and $\boldsymbol{v}_i$. $\boldsymbol{F}_i$ is the total force acting on the ion i, which depends on the positions and velocities of all other ions, and on the time t. There are several contributions to this force: the trap potential force $\boldsymbol{F}_i^{\mathrm{trap}}$, the Coulomb interaction force due to all other ions $\boldsymbol{F}_i^{\mathrm{Coulomb}}$, the stochastic force $\boldsymbol{F}_i^{\mathrm{stochastic}}$ [21] resulting from the random interactions of ions with surroundings such as collisions with residual gas, scattered light, electric field noise, and the laser cooling force $\boldsymbol{F}_i^{\mathrm{laser}}$, which acts on the laser-cooled ions only.

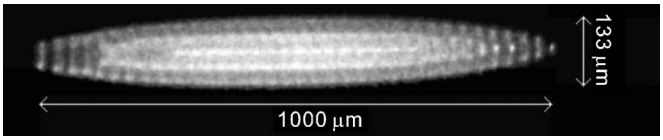

FIG. 1. CCD image of a typical laser-cooled $^9Be^+$ ion crystal in a linear Paul trap containing sympathetically cooled molecular hydrogen ions. The cooling laser propagates to the right, the crystal is at $T_{\mathrm{sec}} \approx 6$ mK and consists of 435 ± 10 $^9Be^+$ and 7 H_2^+ ions, located near the left end of the image symmetry axis.

The linear trap provides an oscillating saddle-shaped potential (voltage amplitude V_0 and angular frequency Ω) which confines the ions in the radial (x-y) plane, while they are confined in the axial (z) direction by a dc trapping field V_{ec}. Near the center of the trap, the trap potential is described by [22]

$$V(x,y,z,t) = \frac{2V_0}{r_0^2}(x^2 - y^2)\cos(\Omega t) + \frac{\kappa V_{\mathrm{ec}}}{2z_0^2}(2z^2 - x^2 - y^2), \tag{2}$$

where r_0 and z_0 are radial and axial dimensions of the trap and κ is a constant determined by the geometry of the trap electrodes. For appropriate trap parameters, in such a potential ions undergo a dominant motion with low-frequency components (secular motion), with a superimposed fast jitter motion (micromotion) of small amplitude in the x-y plane. The secular motion of a single ion can be described as a motion in the harmonic pseudopotential well

$$\psi(x,y,z) = \frac{eV_0^2}{m\Omega^2 r_0^4}(x^2 + y^2) + \frac{\kappa V_{\mathrm{ec}}}{2z_0^2}(2z^2 - x^2 - y^2), \tag{3}$$

with secular resonance frequencies in radial (x,y) and axial directions:

$$\omega_r := \omega_x = \omega_y = \sqrt{\frac{Q}{m}\left(\frac{qV_0}{4r_0^2} - \frac{\kappa V_{\mathrm{ec}}}{z_0^2}\right)}, \quad \omega_z = \sqrt{\frac{Q}{m}\frac{2\kappa V_{\mathrm{ec}}}{z_0^2}}. \tag{4}$$

Here, $q \equiv 2QV_0/mr_0^2\Omega^2$ and Q is the ion charge. A necessary condition for stable trapping of noninteracting ions is $q < 0.908$. In the following, we consider the case $q \ll 1$. For large ion numbers and nonideal trapping conditions (like rf field asymmetries or offset voltages on the electrodes) strong deviations can occur as described in [19].

The Coulomb force $\boldsymbol{F}_i^{\mathrm{Coulomb}}$ is the repulsive force from all other ions confined in the trap, and has the form

$$\boldsymbol{F}_i^{\mathrm{Coulomb}} = \frac{Q_i}{4\pi\varepsilon_0}\nabla \sum_{j=1, j\neq i}^{N} \frac{Q_j \boldsymbol{r}_{ij}}{r_{ij}}, \tag{5}$$

where r_{ij} and $\boldsymbol{r}_{ij}$ are the distance and the unit vector between ion i and ion j, respectively. ε_0 is the permittivity of free space.

In our work, Newton's equations of motion for the trapped ions are numerically solved using the leapfrog algorithm [23]. If the simulations are performed in the pseudopotential approximation ($\boldsymbol{F}_i^{\mathrm{trap}} = -Q_i \nabla \psi$), the integration time step Δt can be much longer and the computing time is much shorter compared to the case when micromotion is considered (where $\boldsymbol{F}_i^{\mathrm{trap}} = -Q_i \nabla V$). The specific time steps used for simulations depend on the rf frequency Ω of the considered ion trap. We operate two traps—one for experiments with laser-cooled $^{138}Ba^+$ ions [$\Omega = 2\pi(2.5\ \mathrm{MHz})$], another for $^9Be^+$ ions [$\Omega = 2\pi(14.2\ \mathrm{MHz})$]. For simulations of ion crystals in the barium trap the time steps typically are 2 or 10 ns when micromotion is included, and 400 or 500 ns in the pseudopotential case. For the beryllium trap, the time steps have to be shorter, 1 ns and 50 ns for the micromotion and the pseudopotential cases, respectively. Typical simulated time intervals are in the order of milliseconds, leading to computing times up to weeks for the largest systems (3000 particles). Note that the computing time scales approximately as N_{tot}^2, since the calculation of $\boldsymbol{F}_i^{\mathrm{Coulomb}}$ is the most time-consuming part of the simulation.

Our simulation program "SOSC" (simulation of sympathetic cooling) is implemented in Delphi, runs on ordinary Windows PCs and comes with a graphical user interface.

B. Heating effects

In order to characterize the temperature of an ion crystal one has to distinguish between the energy contributions of the micromotion and of the secular motion. The secular energy, where the micromotion oscillation is averaged out, can be taken as an indication of the temperature of the ion crystal, since it arises from the disordered motion of the interacting ions in the time-averaged trap potential. In contrast, the micromotion contribution to the total energy arises from a driven motion, which is limited to the radial direction in the linear ion traps considered here.

The root-mean-square (rms) velocity, $(v_{i\alpha}^{\mathrm{rms}})^2 = (1/J)\Sigma_{j=1}^{J} v_{i\alpha}^2$, is a measure of the kinetic energy averaged over one rf period. $\alpha = x,y,z$ denotes the directions; j and J are the time step number and the number of time steps in one rf period, respectively. The secular velocity is defined by averaging over one rf period, $\bar{v}_{i\alpha} = (1/J)\Sigma_{j=1}^{J} v_{i\alpha}$.

Figure 2 shows histograms of these two quantities for a large ensemble of ions of the same species. The histograms are averages over single-period histograms. The secular velocities $\bar{v}$ show a Gaussian distribution corresponding to that of a gas in thermal equilibrium, and the variances of the axial and radial velocities are equal. Thus a unique secular temperature of an ion ensemble can be introduced as

$$\frac{2}{3k_B}E_{\mathrm{sec}} = T_{\mathrm{sec}} = \frac{1}{3Nk_B} m \sum_{i}^{N} (\langle \bar{v}_{ix}^2 \rangle + \langle \bar{v}_{iy}^2 \rangle + \langle \bar{v}_{iz}^2 \rangle), \tag{6}$$

where $\langle \cdots \rangle$ denotes an average over many rf periods and N is the total ion number.

The time-averaged micromotion energy can be defined as the difference between time-averaged total energy

$$E_{\mathrm{tot}} = \frac{1}{2N} m \sum_{i}^{N} [\langle (v_{ix}^{\mathrm{rms}})^2 \rangle + \langle (v_{iy}^{\mathrm{rms}})^2 \rangle + \langle (v_{iz}^{\mathrm{rms}})^2 \rangle], \tag{7}$$

and the secular energy E_{sec}. Unlike in the case of ion strings on the trap axis (where micromotion would be zero), in the large ensembles in the mK regime considered here, the total energy is a few orders larger than the secular energy, as a comparison of the histograms in Fig. 2(b) indicates. Thus, the micromotion energy can be approximated by the total energy [24].

The micromotion leads to rf heating—an ion-ion interaction during which micromotion energy is transferred to secular energy [15,25–27]. Figure 3 shows how the secular temperature of an ion ensemble rises due to rf heating only. In this simulation, where micromotion is included, an ensemble

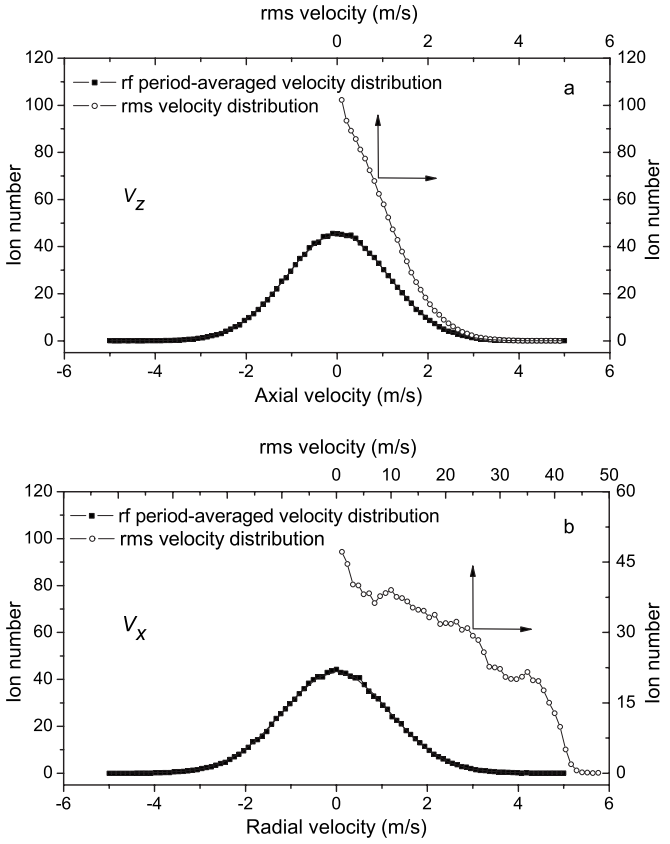

FIG. 2. Velocity distributions for an ion ensemble containing 1250 $^{138}Ba^+$ ions at $T_{sec} \approx 13$ mK. The rf averaged and rms velocity distributions are shown for (a) the axial and (b) a radial direction. The simulation included micromotion.

of 1250 $^{138}Ba^+$ ions was set to $T_{sec}=600$ mK, then all cooling and heating sources were switched off and the ensemble was left evolving. As rf heating rises with temperature [15], the temperature increase is slow in the beginning, with a rf heating rate $dT_{sec}/dt \approx k_B(2.93\ \mathrm{K/s})$ at 600 mK, and much faster at higher temperatures, with a rate of $\approx k_B(39.29\ \mathrm{K/s})$ at 10 K. In our experiments, the ion ensembles are generally in the crystal state at temperatures from 5 to 100 mK with small q parameters and low ion numbers (less than 3000 ions). Under these conditions, rf heating is almost negligible [$\ll k_B(1\ \mathrm{K/s})$].

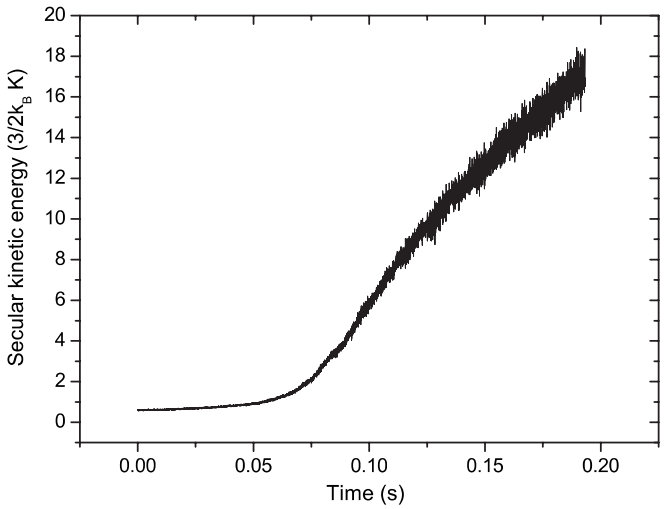

FIG. 3. Rf heating. After the laser cooling is switched off (at $t=0$) the secular energy of an ion ensemble (1250 $^{138}Ba^+$ ions, $q=0.119$) rises in a nonlinear fashion from ≈600 mK to ≈17 K in about 0.2 s purely due to rf heating.

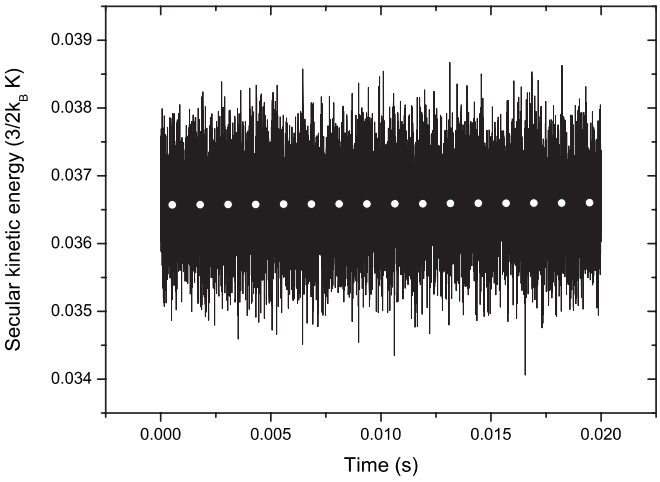

FIG. 4. Rf heating in an imperfect trap. The simulation includes an additional rf phase shift of 0.1 rad between neighboring electrodes and a dc offset of 5 V in x direction applied to the central electrodes. The plot shows the temperature of an ion ensemble (1250 $^{138}Ba^+$ ions, $q=0.083$) in the absence of laser cooling and other heating. A linear fit (open circles) yields a heating rate of $\approx k_B(0.00234\ \mathrm{K/s})$.

However, trap imperfections as a result of rf phase shifts or stray fields can lead to an increased rf heating [25]. To obtain an upper limit of this effect, in a simulation we implemented an additional rf phase shift of 0.1 rad between neighboring electrodes and a dc offset of 5 V in x-direction applied to the central electrodes (see [3,28] for details on our linear Paul traps). An ensemble of 1250 $^{138}Ba^+$ ions was set to $T_{sec}=36.5$ mK, and then let evolve with cooling and heating sources switched off. As Fig. 4 shows, the rf heating is very low [$\approx k_B(0.00234\ \mathrm{K/s})$] in this typical temperature regime, even in the case of a strongly imperfect trap.

Another heating source which can be substantial also at low temperatures are collisions with residual gas. At low temperatures ($T<300$ K) the most important ion-neutral interaction arises from an induced dipole attraction which has a potential $\varphi=-(\alpha/2)(e/4\pi\epsilon_0 r^2)^2$ [29] for a singly charged ion. Here α is the polarizability of the neutral atom or molecule, e the electron charge, and r the radial separation. Using classical collision theory one can derive an expression for the ion-neutral collision heating or cooling rate [29] as

$$h_{\mathrm{coll}} = \frac{3(2.21)}{4}\frac{ek_B}{\epsilon_0} n_n \sqrt{\alpha\mu}\frac{T_n - T_c}{m_n + m_c}, \tag{8}$$

and the momentum transfer collision rate

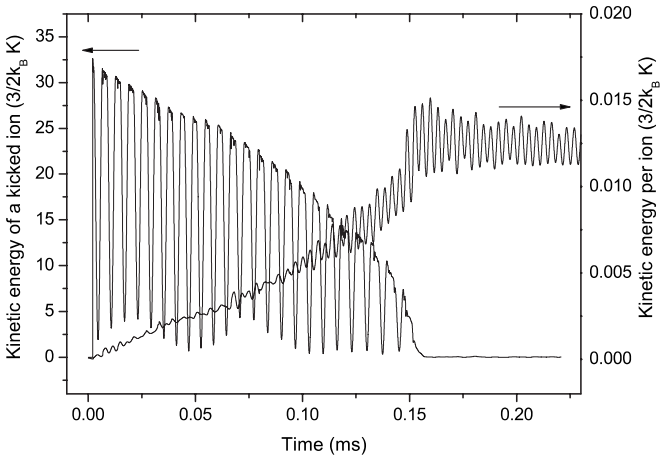

FIG. 5. Ion-neutral head-on collision. After its collision with a neutral helium atom a barium ion gradually transfers its gained kinetic energy (left scale) to the whole ion ensemble, whereupon the kinetic energy per ion (right scale) increases. The simulation was performed without micromotion.

$$\gamma_{\text{elastic}} = \frac{2.21}{4}\frac{e}{\epsilon_0}n_n\sqrt{\frac{\alpha}{\mu}}, \tag{9}$$

where n_n is the particle density of the neutral gas, m_n (m_c) and T_n (T_c) are the masses and temperatures of the neutrals (charged particles), and $\mu = m_n m_c/(m_n+m_c)$ is the reduced mass.

For example, in a background gas of N_2 at 300 K and a pressure of 1×10^{-9} mbar the average $^{138}Ba^+$-N_2 elastic collision rate is $\gamma_{\text{elastic}} \approx 0.017\ \text{s}^{-1}$. In each collision the average energy transfer is $\approx k_B$ (128 K), leading to a heating rate $h_{\text{coll}} = k_B(2.2\ \text{K/s})$, which increases linearly with the residual gas pressure.

Finally, electric noise on the electrodes can lead to heating [30].

C. Modeling of heating effects

Consider the case of an ion colliding with a residual gas atom or molecule. The velocity magnitude change can exceed 100 m/s. This is so strong that the ion leaves the ion crystal and moves in the whole trap volume. Each time the ion passes through the ion cluster, it transfers some energy to it, with the energy loss rate being the lower, the faster the ion is [18]. Figure 5 shows the kinetic energies of an ion ensemble of 1249 barium ions and of a single ion after the latter has suffered a head-on collision with a helium atom of $\frac{3}{2}k_B(300\ \text{K})$ kinetic energy. The colliding barium ion suddenly gains a large velocity (76.8 m/s) and starts to oscillate in the trap. Its kinetic energy is periodically transformed into potential energy and back. It gradually leaks to other ions until the whole ensemble reaches an equilibrium state with increased potential and kinetic energies per ion. For a typical crystal, as considered here, the thermalization time is $\tau \approx 0.2$ ms.

The collision heating of an ensemble of N ions will be essentially continuous if the time between two collisions in the whole ensemble, $1/N\gamma_{\text{elastic}}$, is smaller than the thermalization time τ, i.e., for ion numbers $N > 1/(\gamma_{\text{elastic}}\tau)$. For a typical value of $\gamma_{\text{elastic}} = 0.02\ \text{s}^{-1}$, this condition is fulfilled for $N > 250\,000$ ions. Thus, much smaller ensembles can appear significantly colder in a single CCD image than the actual time-averaged temperature, if the CCD exposure time is less than $1/(N\gamma_{\text{elastic}})$. With a typical exposure time of 2 s this is the case for $N < 25$ ions. Indeed, our experience is that small clusters show a lower temperature (as found from the CCD images) than larger ones.

Ion ensembles considered here are usually large ($N > 2000$) and the CCD camera exposure times are long enough, so that collision heating due to the relatively rare collision events (as well as other heating processes) can be implemented by a more continuous heating in the simulations. Choosing more frequent velocity kicks with appropriately low velocity kick magnitudes, computing time can be saved because equilibrium states are reached much faster (within a few ms of simulated time).

Thus, we consider a model in which each ion experiences a velocity kick $\boldsymbol{w}_k$ at each integration step with a fixed magnitude in a random direction. It is described by the function

$$\boldsymbol{w}_k(t) = v_{l,0}\hat{\boldsymbol{w}}_k(t). \tag{10}$$

Here, $v_{l,0}$ is a constant velocity kick magnitude that in general may differ from species to species l, $\hat{\boldsymbol{w}}_k(t)$ is a unit vector whose direction is chosen randomly for each ion at each integration step. The average change in kinetic energy per ion for a particular species l from one integration step (duration Δt) to the next is, in absence of any forces,

$$\langle \Delta E_l \rangle = \frac{m_l}{2}\langle \boldsymbol{v}_k^2(t+\Delta t) - \boldsymbol{v}_k^2(t)\rangle = \frac{m_l}{2}\langle 2\boldsymbol{v}_k(t)\boldsymbol{w}_k(t) + \boldsymbol{w}_k^2(t)\rangle$$

$$= \frac{m_l}{2}\langle \boldsymbol{w}_k^2(t)\rangle, \tag{11}$$

since the ion velocities and the velocity kicks are uncorrelated [31,32]. The kinetic energy increase rate per ion (heating rate) is therefore

$$h_l = \frac{\langle \Delta E_l \rangle}{\Delta t} = \frac{1}{2}m_l v_{l,0}^2/\Delta t. \tag{12}$$

In a more general approach, at each integration step $N_{l,\text{kick}}$ ions of each species are randomly chosen and given random velocity kicks. Then, the heating rate is

$$h_l = \frac{1}{2}m_l\frac{N_{l,\text{kick}}}{N_{l,\text{total}}}\tilde{v}_{l,0}^2/\Delta t. \tag{13}$$

Here, $N_{l,\text{total}}$ is the total number of ions of species l, and the $\tilde{v}_{l,0}$ are the $v_{l,0}$ from Eq. (12) chosen in such a way that h_l is equal to h_{coll}.

Thus a given heating rate can be implemented in different ways—by frequent kicks with small velocity kick amplitudes $v_{l,0}$ or by rare ones with large amplitudes. Figure 6 illustrates this. Here, an ensemble of 1250 barium ions was set to 0 K and then let evolve without any cooling and with a heating rate $h = k_B(11.95\ \text{K/s})$. In the first case (open circles) all ions were kicked after each time step ($\Delta t = 500$ ns) with kick

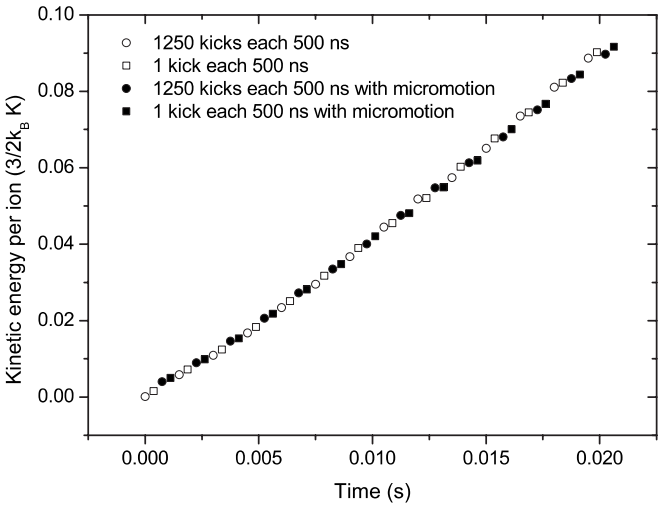

FIG. 6. Heating with velocity kicks. A specific heating rate was realized with different velocity kick frequencies $N_{l,\mathrm{kick}}/(N_{l,\mathrm{total}}\Delta t)$ by adjusting kick magnitudes accordingly (open circles and squares). The filled circles and squares show the heating in presence of micromotion.

magnitude $v_0=2.68\times10^{-2}$ m/s and in the second case (open squares) just one ion ($N_{l,\mathrm{kick}}=1$) was kicked per time step, with an appropriately higher magnitude $\tilde{v}_0=0.949$ m/s. As expected, in both cases the rate of increase of the kinetic energy per ion is the same. Additionally, these simulations were performed including micromotion in the time-dependent trap potential $V(x,y,z,t)$ [see Eq. (2)], but using the same kick parameters (filled circles and squares). We find the same heating rate. This is due to the fact that the implemented kicks change the velocities of the ions (several m/s, see Fig. 2) only by small amounts, and thus preserve the phase of their micromotion. Thus rf heating is negligible for secular temperatures $\ll$(1 K). Note that in the simulation velocity kicks of constant magnitude have been used, and not a Maxwellian distribution.

The employed heating procedure does not lead to a linear increase in time of the kinetic energy per ion, as naively expected from Eq. (12). This is due to the fact that the definition considers an equilibrium state of heating and cooling effects, whereas Fig. 6 shows a dynamic process with heating only. Here, the rising temperature leads to an increase of the ion ensemble's volume whereupon the potential energy of the ensemble increases nonlinearly. Due to energy conservation it is the total energy of the ensemble which increases linearly with time when applying a certain heating rate. Both the kinetic energy and the potential energy increase nonlinearly. This is shown in Fig. 7 for an ensemble of 1250 barium ions heated with $h=k_B(11.95\ \mathrm{K/s})$ without any cooling. The gray curve shows the nonlinear change of the kinetic energy, and the light gray curve the one of the potential energy. Here, the ground potential energy (the mutual Coulomb energy of the ions at zero temperature plus their trap potential energy), $k_B(70.75\ \mathrm{K})$, was set as reference energy. The black curve is the total energy change due to the velocity kicks. It is linear with a slope of $k_B(11.6\ \mathrm{K/s})$, which agrees well with the applied heating rate h.

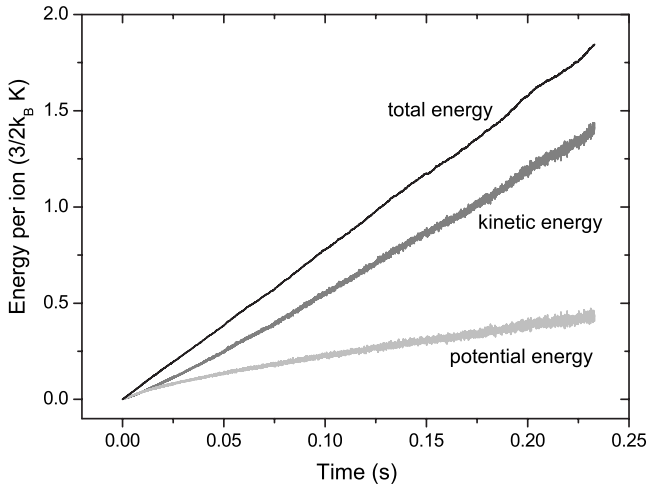

FIG. 7. Energy distribution. The total energy per ion (black) increases linearly according to the implemented heating rate in the velocity kick model (micromotion not included). However, the kinetic (gray) and the potential (light gray) energy grow nonlinearly due to a growth of the ion ensemble's volume.

The appropriateness of the kick model can also be verified by comparing theoretical collision heating rates with those extracted from experimental data via simulations.

Experimentally, CCD images of an ensemble of $^{138}Ba^+$ ions at different N_2 pressures were taken. Assuming a realistic cooling rate $\beta=2\times10^{-22}$ kg/s (see Sec. II D), at each pressure we fitted the heating rate that yields the best agreement of simulated and experimental image. Figure 8 shows these experimental values (circles) together with the collision heating rate h_{coll} (black line) for $^{138}Ba^+$ ions and N_2 molecules, rising linearly with the N_2 pressure. Here, T_n-T_c [see Eq. (8)] was set to 300 K. For pressures above 1×10^{-9} mbar, the experimental values agree well with the theoretical heating rate given by Eq. (8), with $\alpha_{N_2}=4\pi\epsilon_0(1.76\times10^{-24}\ \mathrm{cm}^3)$.

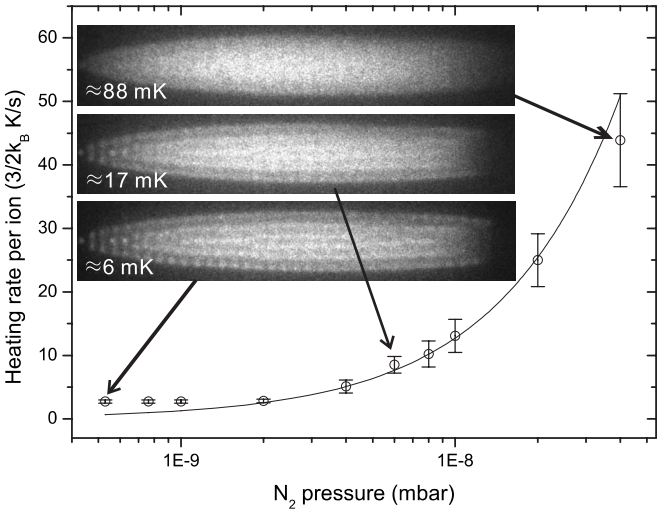

FIG. 8. Collision heating. The black curve shows the theoretical collision heating rates for collisions of $^{138}Ba^+$ ions and N_2 molecules, the circles show the heating rates extracted from the experiment.

The agreement is not complete at the lowest pressures. To a lesser extent, this could be due to the finite spatial resolution of our imaging system, which naturally leads to blurring of the crystal. However, we believe that other heating sources besides the considered rf and collision heating are present, such as electric field noise and possibly additional collision heating due to ion micromotion. As we cannot quantify them, they are not implemented in our simulations directly, but their effect can be included in the velocity kick model as a pressure-independent contribution to $\tilde{v}_0$.

D. Cooling model

As laser cooling force $\boldsymbol{F}_i^{\text{laser}}$ we consider a linear viscous damping force plus a constant light pressure force

$$\boldsymbol{F}_i^{\text{laser}} = -\beta_i \dot{\boldsymbol{r}}_i + \boldsymbol{F}_i^{\text{lp}}. \tag{14}$$

This damping force would require three mutually orthogonal laser beams. The light pressure force $\boldsymbol{F}_i^{\text{lp}}$ pushes the laser cooled ion ensemble in the laser beam direction and gives a spatial offset from the potential well center. The cooling force reduces the velocity magnitude of the laser-cooled ions, so the kinetic energy change rate per ion is

$$\Delta E_i = \frac{1}{2}m_i v_i^2(t+\Delta t) - \frac{1}{2}m_i v_i^2(t) = \frac{1}{2}m_i\left(1-\frac{\beta\Delta t}{m_i}\right)^2 v_i^2(t) - \frac{1}{2}m_i v_i^2(t) = \frac{1}{2}m_i v_i^2(t)\left[\left(\frac{\beta\Delta t}{m_i}\right)^2 - 2\frac{\beta\Delta t}{m_i}\right]. \tag{15}$$

Because the friction coefficient β is very small ($\beta_{\max} \approx \pi^2\hbar/\lambda^2 \approx 4\times 10^{-21}$ kg/s) for transitions at optical wavelengths λ [17]), the first term in the parenthesis can be neglected. Thus the kinetic energy decrease rate per ion ("cooling rate") of a species l is

$$c_l = \frac{\langle \Delta E_i\rangle}{\Delta t} = -\frac{2\beta}{m_l}\left\langle \frac{1}{2}m_l v_i^2(t)\right\rangle = -\frac{2\beta}{m_l}\langle E\rangle_l. \tag{16}$$

The temperature of the ion species l, T_l, is obtained from $\frac{3}{2}k_B T_l = \langle E\rangle_l$, where $\langle E\rangle_l$ is the time- and ensemble-averaged kinetic energy. The temperature decrease rate of an ion ensemble l is

$$\frac{dT_l}{dt} = -\frac{2\beta}{m_l}T_l. \tag{17}$$

This holds when the cooling is along all three spatial directions simultaneously. If the ion ensemble is cooled by only one laser beam along the axial direction z, then in the expression for c_l in Eq. (16) v_i is to be replaced by $v_{i,z}$, and E_i by $E_{i,z}$. Thus, the temperature reduction rate should be divided by 3 to get

$$\frac{dT_l}{dt} = -\frac{2}{3}\frac{\beta}{m_l}T_l. \tag{18}$$

Indeed, cooling with only one laser beam is sufficient to reduce the secular motion of the ions in all dimensions, because their mutual Coulomb interaction leads to a fast thermalization. This is also conventionally implemented in experiments. Figure 9 shows an ensemble of 1250 barium ions cooled with a friction coefficient $\beta = 2\times 10^{-22}$ kg/s along the axial direction without applying any heating. The secular kinetic energy per ion in radial (x or y) and axial (z) direction decreases by two orders of magnitude within less than 10 ms. As the radial secular motion is reduced indirectly, its decrease is slightly slower than that of the axial secular motion which is most obvious in the mK regime.

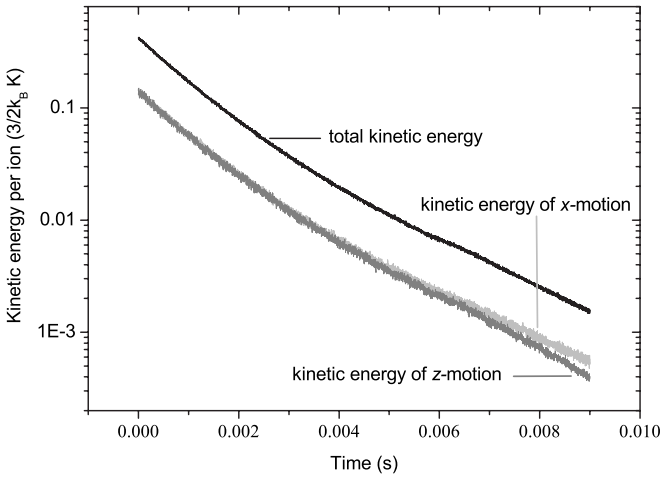

FIG. 9. Simulation of viscous cooling of an ion ensemble. 1250 barium ions are cooled by only one laser beam along the trap axis ($\beta = 2\times 10^{-22}$ kg/s, no heating applied, micromotion not included). The kinetic energy is effectively reduced in all dimensions.

E. Simulation of CCD images

When taking CCD images of laser-cooled ion ensembles our typical exposure times are in the order of 0.5 to 2 s. During that time the ions' trajectories span several meters due to their residual secular kinetic energy (see Fig. 10) [33]. As a result, the images appear blurred and can be considered

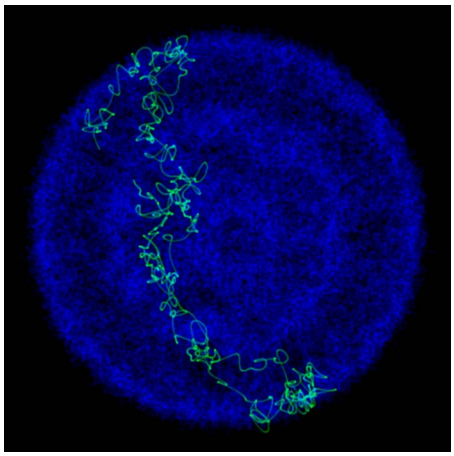

FIG. 10. (Color online) Diffusion in an ion crystal. In this axial view of a time-averaged ion crystal at 6 mK the trajectory of a single ion is shown in green. During the "exposure time" of 5 ms the ion diffuses through the whole ensemble. This simulation did not include micromotion, no heating and cooling was applied.

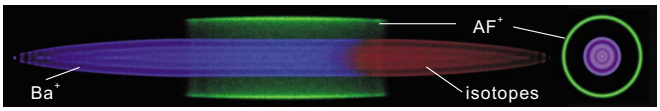

FIG. 11. (Color online) Spatial structure of a multispecies ion crystal. The ion crystal consists of 830 laser-cooled $^{138}Ba^+$ ions (blue), 420 singly charged barium isotopes (red), and 200 protonated AlexaFluor350 molecules (blue). The left image is a radial view; the right is an axial view. The overall length is 1.7 mm; the diameter is 300 μm.

as probability density plots, rather than as images of individual particles.

To reproduce these CCD images by simulations, the positions of all ions for every time step of the simulation are projected to a plane perpendicular to the desired line of sight. (In our setups, the line of sight is radial, i.e., perpendicular to the z-axis and at 45° to the x and y axis.) A density plot of this plane corresponds to a CCD image observed.

A completely realistic simulation of the CCD images would require simulated times as long as the exposure times and a more accurate implementation of the ions' collisions with the background gas, i.e., rare and strong collisions (compare Sec. II C), leading to long computing times. With our more continuous velocity kick model equilibrium states are reached after simulated times of a few ms and the experimental CCD images can be reproduced with good agreement. The reason for this are the CCD exposure time, which is much longer than the thermalization time, and the short intersite diffusion time for the temperatures considered here.

In contrast to the experiment, simulations can also visualize ions which are not laser-cooled and therefore do not fluoresce. Figure 11 shows a multi-species ion crystal [4] consisting of 830 laser-cooled $^{138}Ba^+$ ions, 420 singly charged barium isotopes (m=137 amu), and 200 singly protonated AlexaFluor350 molecules (m=410 amu). Because the radial confinement for ions with a higher mass-to-charge ratio is weaker, the heavier $^{410}AF^+$ ions are located around the $^{138}Ba^+$ ions, as shown in the axial view on the right-hand side of Fig. 11. The lighter barium isotope ions would arrange inside the $^{138}Ba^+$ crystal and form a core (see Fig. 16 for the much lighter CO_2^+ ions), but as the mass difference is small and the light pressure pushes the $^{138}Ba^+$ ions to the left, they arrange on the right side of the crystal and only slightly leak into the $^{138}Ba^+$ crystal.

III. APPLICATIONS

A. Sympathetic heating and cooling

If other ion species are confined in the trap simultaneously with laser cooled ions, they can be sympathetically (indirectly) heated or cooled via their mutual long-range Coulomb interaction.

To quantify this interaction, Fig. 12 shows a simulation of the various forces acting on the multispecies ion ensemble from Fig. 11. Initially, all species were set to a (secular) temperature of 0 K and in the spatial configuration of the lowest potential energy. Then a heating rate of h_{138Ba}

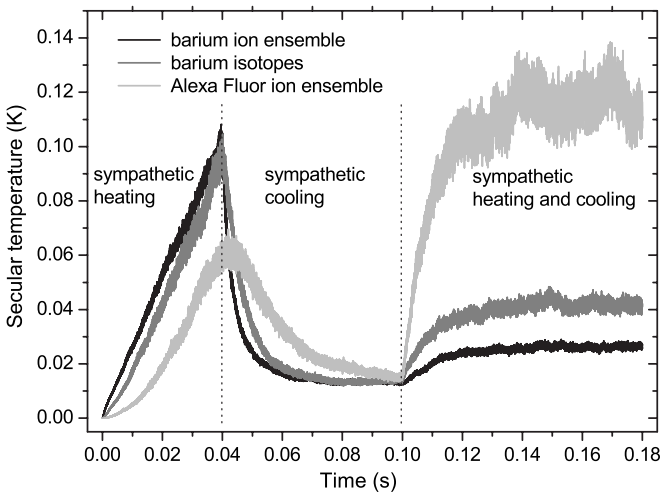

FIG. 12. Sympathetic heating and cooling in a multispecies ion ensemble. The ion composition is the same as in Fig. 11. After all species were set to a secular temperature of 0 K, heating is implemented only for the $^{138}Ba^+$ ions starting at t=0 s, and the other ions are sympathetically heated. At t=0.04 s the laser cooling of $^{138}Ba^+$ is added, and the $^{138}Ba^+$ temperature decreases. The $^{138}Ba^+$ ions now sympathetically cool the other ions, and the ensemble reaches an equilibrium state at nonzero temperature. Finally at t=0.1 s, heating is also turned on for the barium isotopes and the $^{410}AF^+$ ions, which increases the temperatures of all species until they reach the equilibrium state. This simulation did not include micromotion.

$=k_B$(11.55 K/s) is applied to the $^{138}Ba^+$ ions. Their temperature increases (black curve), and due to the sympathetic interaction the temperatures of the other two ion species increase as well. Because the mass-to-charge ratio of the barium isotope ions is very close to that of the $^{138}Ba^+$ ions, these two species couple very well and the energy transfer efficiency is high. Thus, the temperature of the barium isotope ions (gray curve) closely follows that of the $^{138}Ba^+$ ions. However, for the $^{410}AF^+$ ions the coupling to the $^{138}Ba^+$ ions is lower due to their larger radial separation caused by the significant mass-to-charge ratio difference. So, their temperature increase is weaker (light gray curve). After 40 ms the laser cooling is switched on with a friction coefficient $\beta=2\times10^{-22}$ kg/s. As the cooling of the $^{138}Ba^+$ ions is higher than the heating h_{138Ba}, their temperature starts to decrease. When their temperature gets lower than that of the other species, these start to be cooled sympathetically until all species reach an equilibrium state with nearly equal temperatures. At t=100 ms, realistic conditions are established by switching on the heating for the barium isotopes and the $^{410}AF^+$ ions (with heating rates of k_B(11.47 K/s) and k_B(25.14 K/s), respectively). Their temperatures increase above the $^{410}AF^+$ temperature, which in turn causes a sympathetic heating of the $^{138}Ba^+$ ions. Finally, the whole ensemble reaches an equilibrium state with stable, but species-dependent temperatures, i.e., temperature gradients are present.

B. Determination of ion numbers

Shape and structure of an ion crystal are determined by the trap potentials applied, the number of ions, the ion spe-

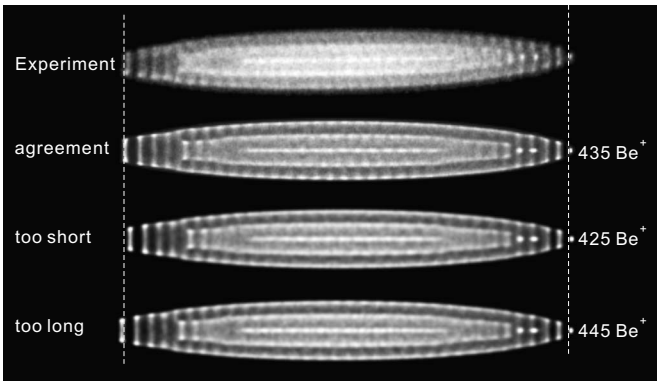

FIG. 13. Determination of ion numbers. The experimental image of a beryllium ion crystal is compared with simulated images with different ion numbers. The best fit is achieved for a number of 435 $^9Be^+$ ions.

cies, the light pressure force, and the temperatures. Ion numbers and temperatures can be obtained from comparison of experimental and simulated images of the ion crystals.

Firstly, the number of the trapped ions are determined. For ion crystals consisting of laser-cooled ions only the procedure is as follows: As the magnification of the imaging system is known, one adjusts the number of ions until the simulated crystal has the same dimensions as the observed one. Here (mK regime), the volume of the crystal is not significantly influenced by the temperature of the ions. Therefore, the ion number can be fit without considering the temperature.

For ion crystals containing sympathetically cooled ion species in addition, the determination of ion numbers is more complicated. Ions with higher mass-to-charge ratios arrange around the laser-cooled ion ensemble and therefore modify its shape. If the species is known and the mass-to-charge ratio is still close to that of the laser-cooled ions, one can find its number by reproducing the observed deformation. However, for a species with a much higher mass-to-charge ratio, the deformation induced is not sufficient (see Figs. 11 and 16). A reliable determination of the ion numbers is by extraction from the trap and counting [4], but this is a destructive method. As ions with a lower mass-to-charge ratio are located inside the laser-cooled ensemble and form a core, their number can be determined, in a nondestructive manner, from the size of the core.

In both cases, it is essential to consider the light pressure force which shifts the laser-cooled ions out of the trap center and causes strong asymmetries. For example, the beryllium ion crystal shown in Fig. 1 contains H_2^+ ions that are located on the left side of the crystal, because the beryllium ions are shifted to the right. To determine the ion numbers in this crystal we simulated crystals with different ion numbers and compared them with the experimental CCD image (see Fig. 13). The best fit is achieved for 435 ± 10 $^9Be^+$ and 7 H_2^+ ions, when a light pressure force of 8×10^{-21} N is assumed.

C. Temperature determination of laser-cooled ions

In order to determine the temperature of the laser-cooled ions, a series of ion crystals at different temperatures is simulated and visually compared with the experimental CCD image. Due to scattered light and the limited resolution of our imaging system the experimental CCD images look blurred. Thus, the crystals appear warmer than they actually are. There are, however, details in the crystal structure, which are used to find the closest temperature. In Fig. 14, for example, the experimental image of a beryllium crystal (lowermost image) shows two concentric ellipsoidal shells with a string in the middle. The string displays discrete spots which are, comparing with the simulated images above, only visible for temperatures lower than 8 mK. But, these spots are not as distinct as in the simulated image at 5 mK. Thus, the best fit indicates a temperature of 6 mK.

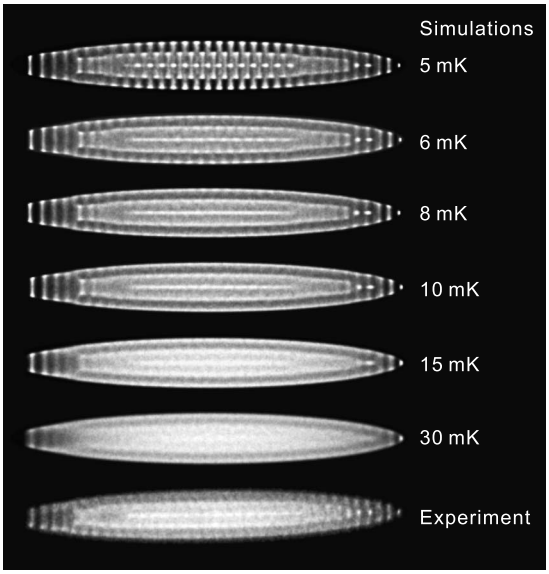

FIG. 14. Temperature determination of laser-cooled ions. A series of simulated ion crystals at different temperatures is compared to the experimental CCD image (bottom, same as Fig. 1). The best agreement is achieved for a temperature of about 6 mK.

As discussed above, these discrete spots usually do not correspond to single or individual ions, but to a high probability density for ions at a certain location during the exposure time, except for special sites and very low temperature.

In contrast to the experiment, in the simulations one can image ion crystals from any direction and with arbitrary magnification. Even specific sites of the crystals can be studied in detail. For example, Fig. 15(a) shows the spatial radial distribution of the spot at the right end of the beryllium crystal shown in Fig. 1. The spatial distribution has a Gaussian shape and a full width at half maximum of 6 μm. Figure 15(b) shows the spatial distribution of the neighboring two spots. They cannot be ascribed to two ions, but to an average of three ions moving diffusively and due to residual rotation of the crystal around the z axis.

D. Temperature determination of sympathetically cooled ions

The temperature of sympathetically cooled ions cannot be determined as described above, because they do not fluoresce and are therefore invisible to the CCD camera. In order to find their temperature, two CCD images are required. One is

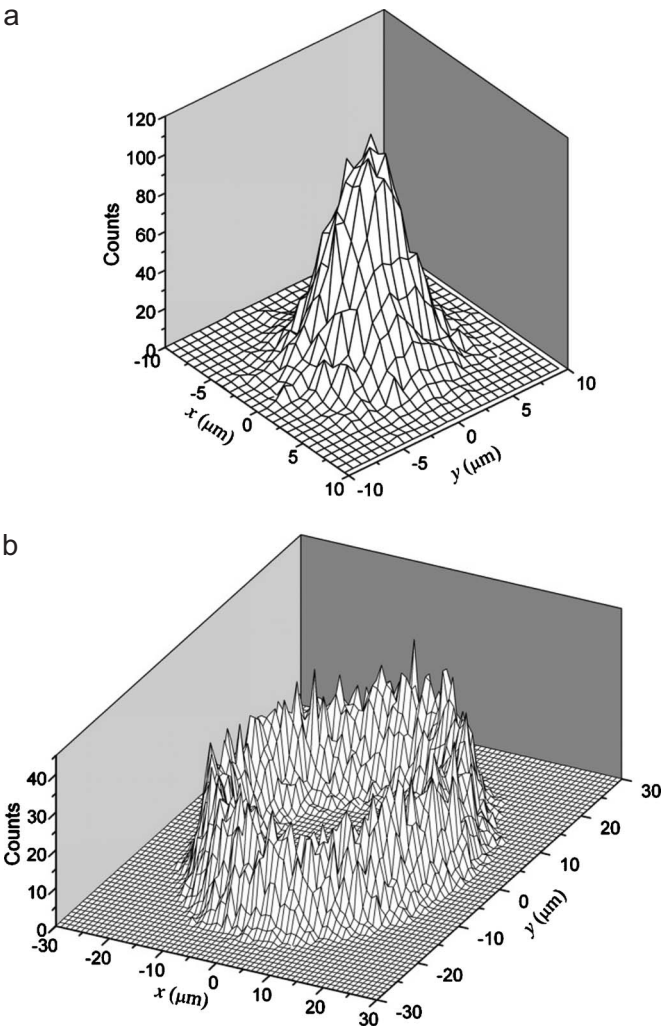

FIG. 15. Probability density of ion trajectories within particular slices $(z_0-\Delta z, z_0+\Delta z)$ of the crystal. (a) For the right end spot and (b) for the two neighboring spots of the beryllium crystal in Fig. 1 (T_{sec}=6 mK). The simulated time is 200 000 time steps of 50 ns.

taken when the laser-cooled and the sympathetically cooled ions are trapped together, the other is taken when there are only the laser-cooled ions, i.e., before loading or after extracting the sympathetically cooled ions. The temperature of both ion ensembles is different, as the heating rate h_{sc} of the sympathetically cooled ions acts as an additional heating source for all ions. By simulating the CCD image of the pure laser-cooled ion ensemble its heating rate h_{lc} is found. In the simulation of the whole ensemble h_{lc} is kept constant for the laser-cooled species. Then, the heating rate h_{sc} for the sympathetically cooled species is varied in order to heat the laser-cooled ion ensemble to the observed temperature. When the right parameters are found, the temperature of the sympathetically cooled ions can be obtained from the simulation data (an example is shown in [4]).

In principle, a specific temperature of a laser-cooled ion ensemble can be achieved with a continuous set of pairs of appropriate laser-cooling and heating rates. The simulated temperature of the sympathetically cooled ion ensemble strongly depends on the actual laser cooling rate. When a higher laser cooling rate is applied, the heating rates for all involved species need to be increased in order to keep the temperature of the laser-cooled ion ensemble constant at the observed level. However, this leads to a higher temperature of the sympathetically cooled ions as illustrated in the following example: Figure 16 shows a four-species ion crystal consisting of 700 laser-cooled barium ions (blue, 138 amu), 300 barium isotope ions (red, 137 amu), 100 CO_2^+ ions (pink, 44 amu), and 200 singly protonated glycyrrhetinic acid molecules (denoted as GA^+, green, 470 amu). In case (a), the friction coefficient β is set to 1×10^{-22} kg/s. To keep the crystal at 20 mK, the corresponding heating rate for barium ions and isotopes is $\approx k_B$(5.94 K/s). After loading the GA^+ ions, we set their heating rate to $\approx k_B$(8.25 K/s), which heats the barium ion ensemble to 25.6 mK. The temperature of the GA^+ ion ensemble in this equilibrium state is ≈130 mK. In case (b), a higher friction coefficient $\beta=4\times10^{-22}$ kg/s is set. To heat the barium ion ensemble to the same 20 mK and 25.6 mK values, higher heating rates are required: $\approx k_B$(23.9 K/s) for the barium ions and $\approx k_B$(33.6 K/s) for the GA^+ ions. Here, the final equilibrium temperature of the GA^+ ions ensemble is ≈300 mK.

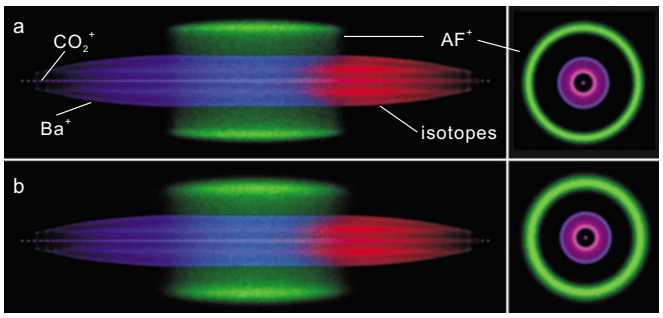

FIG. 16. (Color online) Temperature determination of sympathetically cooled ions. If a higher laser cooling rate is used in the simulations (b), one obtains higher temperatures for the sympathetically cooled species [green (outer)] than in (a).

Thus, in order to obtain a concrete temperature value for the sympathetically cooled ion ensemble, the friction coefficient needs to be determined independently. From laser cooling theory

$$\beta = 2\sum_i \frac{\hbar k_i^2}{2}\Gamma_i \left.\frac{\partial \rho_e}{\partial \Delta_i}\right|_{\Delta_i}. \tag{19}$$

The wave numbers k_i and partial decay rates Γ_i for the laser transitions are constants, whilst the change in the excited state population ρ_e with laser detunings Δ_i is calculated from eight-level Bloch equations using our measured laser saturation parameters and detunings [34]. The value for $^{138}Ba^+$ in our experiments was determined to $\approx 1.75\times10^{-22}$ kg/s in good agreement with [35].

E. Advanced cooling of complex molecular ions

Sympathetic cooling in a Paul trap is most efficient for species with similar mass-to-charge ratio, as their radial separation is small.

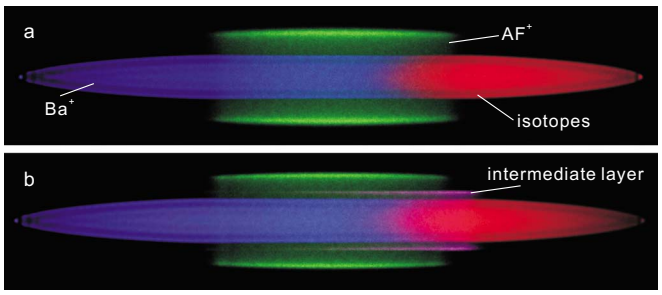

FIG. 17. (Color online) Sympathetic cooling in the presence of an intermediate layer. The images show a multispecies ion ensemble consisting of barium ions (blue, 138 amu), AlexaFluor ions (green, 410 amu), and barium isotope ions (red, 137 amu)—(a) without and (b) with an intermediate species layer (pink, 200 amu), which helps to cool the AlexaFluor ions more efficiently.

In one of our experiments, we used laser-cooled $^{138}Ba^+$ ions to sympathetically cool complex molecular ions with masses of several hundred amu produced with an electrospray ion source [36]. Here, the efficiency of sympathetic cooling is relatively low due to the high radial separation of the ion species and the difference between the temperatures of the species is substantial, as discussed above. A possibility to enhance the sympathetic cooling is the reduction of the mass-to-charge ratio difference, which can be realized by using multiply protonated molecules from the electrospray process. Another option is to raise the trap voltage so as to increase the radial confinement of all ions. However, higher trap voltages also cause a higher rf heating [3,15]. Yet another possibility is a reduction of the total ion number, in order to reduce the repulsive forces between the ion species.

A different approach is to add a (sympathetically cooled) intermediate species layer between the laser-cooled and the sympathetically cooled ions; see Fig. 17. This layer acts as a "conducting layer" and helps to transfer the energy from the sympathetically cooled ions of interest to the laser-cooled ions. Such ions of intermediate mass may be loaded into the trap deliberately or they may be produced by photodissociation of the molecular ions. Figure 18 shows an example for the sympathetic cooling process, in which 200 $^{410}AF^+$ ions are sympathetically cooled by 1250 $^{138}Ba^+$ ions—with and without intermediate layer. Initially, the barium ions are kept at very low temperature (<3 mK) by applying a high cooling rate ($\beta=200\times10^{-22}$ kg/s), while the $^{410}AF^+$ ions are kept at about 490 mK. Then, the heating for the $^{410}AF^+$ ions is turned off and their temperature decreases due to sympathetic cooling. It takes about 40.6 ms to cool them to $\approx$8 mK, but only 8.8 ms when 50 ions with an intermediate mass (200 amu) are added. Thus the sympathetic cooling rate can be substantially increased.

Under realistic conditions (heating effects present), the final temperature of the sympathetically cooled ions can be significantly lower with the intermediate species layer. For the case shown in Fig. 17, 200 $^{410}AF^+$ ions are sympathetically cooled by 830 $^{138}Ba^+$ ions. With an intermediate layer (50 ions, 200 amu), the final temperature of the AlexaFluor ions is reduced from $\approx$114 mK to $\approx$58 mK [see Fig. 17(b)].

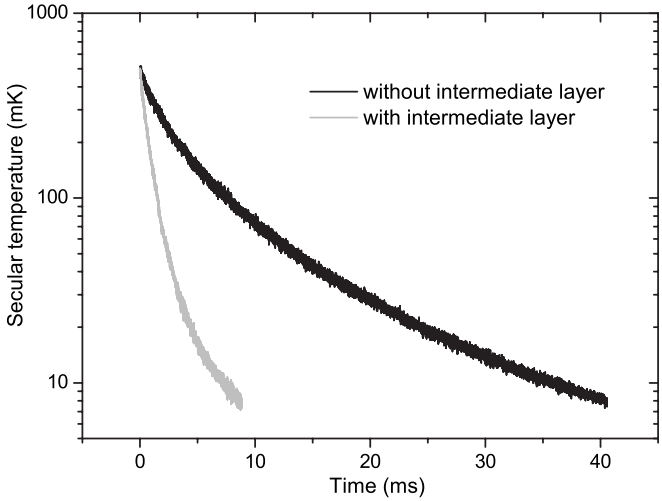

FIG. 18. Sympathetic cooling with an intermediate layer. With an additional intermediate ion species [compare Fig. 17(b)] the sympathetic cooling of the AlexaFluor ions is much faster (gray) than without (black). Note that in this case no heating was applied to the AlexaFluor ions and they would consequently reach the same temperature with or without intermediate layer.

F. Simulation of secular excitation spectra

Experimentally, trapped ion species can be identified by a resonant excitation of their radial secular motion. For this purpose, an additional ac field is applied either to the trap electrodes or to an external electrode. When the excitation field is resonant with the oscillation mode of an ion species, these ions start to oscillate strongly. Consequently, the whole ion ensemble heats up, which causes a change in the laser-cooled ions' fluorescence. By recording the fluorescence during a frequency scan one can obtain a mass spectrum of the trapped ions.

However, the observed frequencies can differ strongly from the calculated values for single ions ω_r [see Eq. (4)]. This is due to the fact that the space charge of all ions and a coupling between trapped species lead to significant shifts of the oscillation frequencies [19,37] and even to the appearance of additional resonances. In a simplified picture, this can be illustrated by comparing the ideal harmonic pseudopotential [see Eq. (3)] with that modified by the space charge of the trapped ions.

In Fig. 19, for example, we consider a cold ion crystal containing 1200 $^{138}Ba^+$ ions and 500 GA^+ ions. The effect of the of the GA^+ ions on the barium ions is shown in Fig. 19(a). The shape of the potential well for a barium ion is almost unchanged, there is only an offset to higher potential energies which does not influence the barium ions' secular frequency. However, as shown in Fig. 19(b), the presence of the barium ions causes a drastic change of the potential well for GA^+ ions. The harmonic pseudopotential is modified to a double well potential. These potential wells are steeper, so that the GA^+ ions have a higher secular frequency. To quantify this, we performed fits with harmonic functions to the wells. The asymmetric double wells can be described by the functions $y=11.5\times10^{-8}(x-160)^2+0.006$ and $y=6.3\times10^{-8}(x-160)^2+0.006$ for the outer part, while the potential

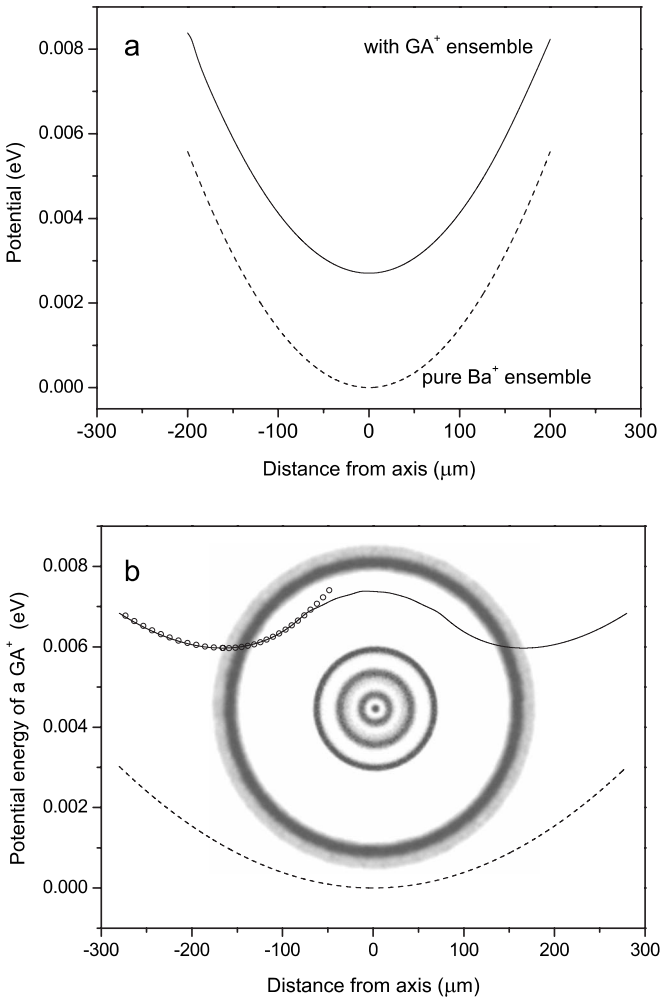

FIG. 19. Space charge effects and trap potentials. Here, we consider a cold ion crystal containing 1200 $^{138}Ba^+$ and 500 GA^+ ions. (a) Potential wells for a single barium ion in the ideal harmonic trap potential (dashed curve) and influenced by the space charge of heavier GA^+ ions (solid curve). (b) Potential well for a single GA^+ ion in the ideal harmonic trap potential (dashed curve) and double well potential caused by the barium ions (solid curve). Superimposed is an axial view of the considered ion crystal.

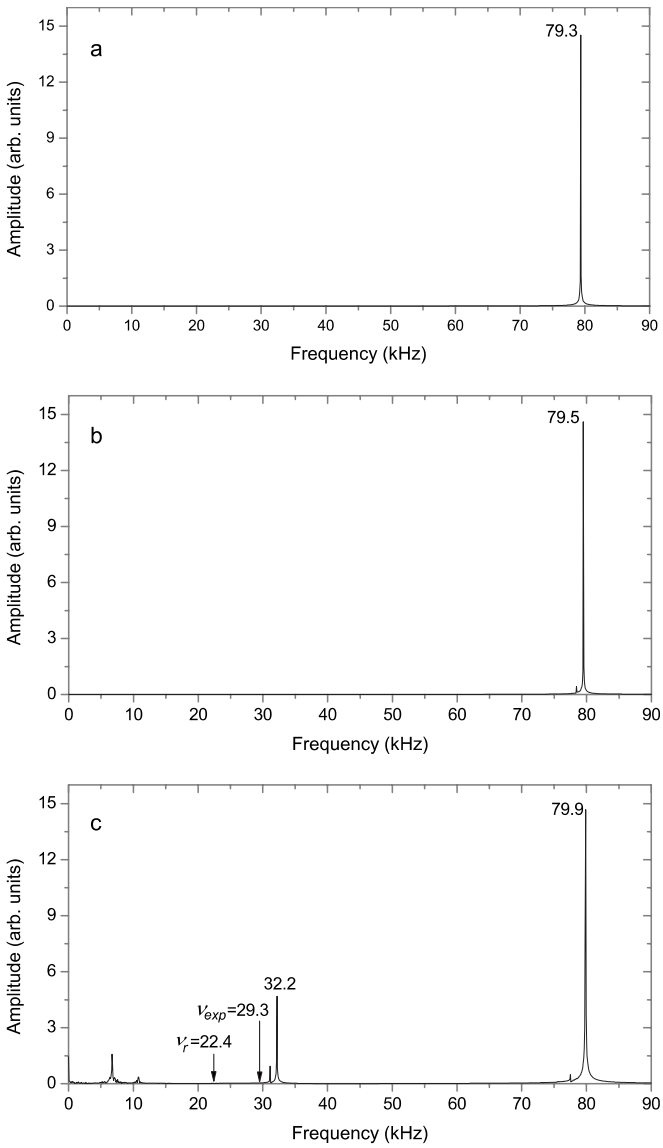

FIG. 20. Simulated radial secular excitation spectra. For equal trap parameters $[q(^{138}Ba^+)=0.091]$ different crystal compositions were considered: (a) only $^{138}Ba^+$; (b) $^{138}Ba^+$ ions and isotopes; (c) $^{138}Ba^+$ ions, isotopes, and GA^+ ions. In (c) ν_r indicates the calculated single-ion frequency for a GA^+ ion and ν_{expt} the experimentally determined value.

for a single trapped GA^+ ion in absence of $^{138}Ba^+$ is described by $y=3.9\times10^{-8}x^2$. Thus, the radial frequency of a GA^+ ion can be up to $\sqrt{11.5/3.9}=1.7$ times higher than the one calculated with the single-ion formula, Eq. (4).

For a more realistic description of the oscillation of an ion species it is necessary to include not only the space charge of the other ion species, but also the space charge of the considered ion species itself. Therefore, in our simulations radial secular excitation spectra are simulated in a simplified manner as follows: The whole ion ensemble is displaced by several μm in a radial direction, then it is released and the center-of-mass positions of all ions are recorded for some time. Finally, a Fourier analysis of these data yields the oscillation modes of the ion ensemble components. Such spectra are shown in Fig. 20 for different ion crystals at equal trap settings $[q(^{138}Ba^+)=0.091]$. For a pure $^{138}Ba^+$ ion crystal [Fig. 20(a)] the simulated frequency $\nu_{\text{sim}}=79.3$ kHz is slightly higher than the calculated single-ion frequency $\nu_r=79.2$ kHz as the barium ions' space charge makes their potential well steeper. In comparison, the spectrum of a crystal consisting of $^{138}Ba^+$ ions and isotopes [Fig. 20(b)] is not much different because the ion masses are quite similar. However, due to the coupling of the ions' oscillation modes there are additional small peaks beside the main peak, which is slightly shifted to a higher frequency of 77.5 kHz. Figure 20(c) shows the excitation spectrum of an ion crystal containing barium ions with isotopes and GA^+ ions. The experimentally determined secular frequency of the GA^+ ions $\nu_{\text{expt}}=29.3\pm1.3$ kHz differs substantially from the single-ion frequency $\nu_r=22.4$ kHz, but is consistent with the simulated value $\nu_{\text{sim}}=32.2$ kHz. The difference may be due to the dependency of the experimental frequency on the excitation

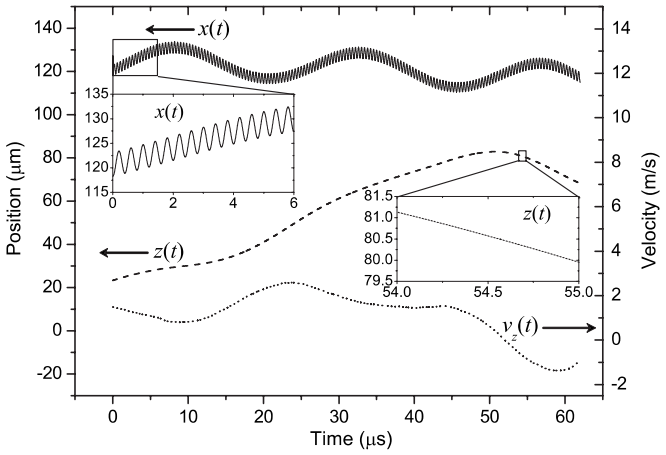

FIG. 21. Micromotion of an individual ion within an ensemble. In a simulation including micromotion the x component of the motion clearly shows the fast micromotion (solid curve, the inset is a magnification). The z component of the motion and the velocity (dashed and dotted curve) do not show any effect of micromotion. The secular temperature of the barium ion ensemble was ≈30 mK.

amplitude in the experiment and the ion numbers (a more detailed description can be found in [19]).

The small additional peaks around 10 kHz in Fig. 20(c) arise from coupling effects of the different species' motion in the multispecies ion ensemble. With our simplified mode excitation model, we cannot characterize in detail these additional modes. This could be done by performing simulations with an additional homogeneous field oscillating at the respective mode frequencies found above and analyzing the amplitudes and phases of the forced oscillations of the individual species.

G. Micromotion effects

Our simulations are a useful tool for the interpretation of experiments with sympathetically cooled molecules. For the determination of ion numbers and temperatures or the simulation of ion crystal structures and secular excitation spectra it is not necessary to include the micromotion in the simulations. To save computing time we solve Newton's equations of motion in the pseudopotential approximation. However, there are some aspects related to micromotion, which cannot be neglected and are considered in the following.

An aspect of relevance for high-resolution spectroscopy is a possible direct coupling of radial micromotion to the axial direction which would lead to the appearance of motional sidebands in the spectrum and thus a loss of spectral resolution. To study this effect, a barium ion from a cold ion ensemble (830 $^{138}Ba^+$ ions, 420 barium isotope ions, and 200 $^{410}AF^+$ ions) was randomly selected and its axial position $z(t)$, one component of the radial position $x(t)$, and its axial velocity $v_z(t)$ were recorded (see Fig. 21). The solid curve $x(t)$ clearly shows the slow radial secular oscillation (≈40 kHz) with the superimposed fast micromotion at the rf driving frequency of 2.5 MHz (see inset). There is no apparent rf oscillation in the axial motion $z(t)$ (dashed curve) and the axial velocity $v_z(t)$ (dotted curve). Thus we find that under the typical conditions considered here (small q parameter, as evidenced by the small amplitude of the micromotion compared to the average radial distance), the micromotion in radial direction does not couple to the axial direction. Nevertheless, at much higher secular temperature, the micromotion causes an increase of the secular energy of both radial and axial motions. The only possibility for an energy transfer of micromotion to the axial motion is an indirect coupling via rf heated ions which distribute their kinetic energy to the axial direction through the thermalization process.

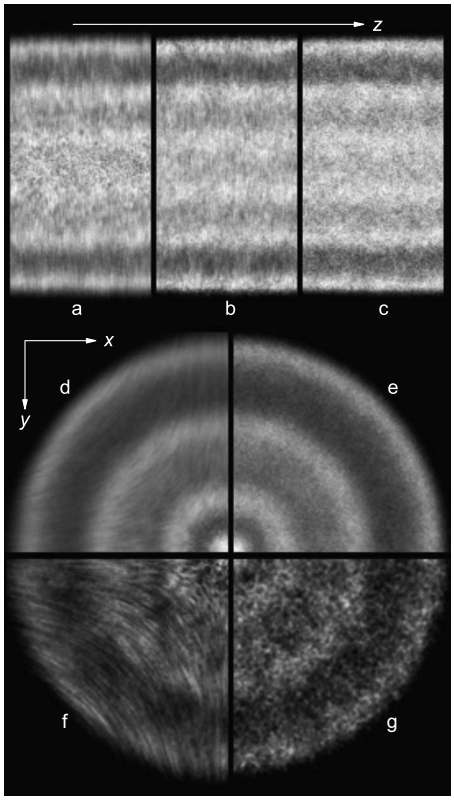

FIG. 22. Micromotion in simulated images. Here, sections from simulated images of a cold ensemble consisting of 500 barium ions are shown—simulated including micromotion [(a),(b),(d), and (f)] and in the pseudopotential [(c),(e), and (g)]. (d)–(g) show sections of axial views, (a)–(c) sections of radial views, while (a) is a view along the x axis and (b) and (c) correspond to the line of sight of the CCD camera (at 45° to the x and y axis). In fact, as the pseudopotential is radially symmetric, (c) shows the view along any angle perpendicular to the axial direction. (f) and (g) show the same as (d) and (e) but for a 20 times shorter simulated time of 0.5 ms in order to highlight the different nature of images from simulations with and without micromotion.

Finally, we have studied the influence of the micromotion on the simulated images. Figure 22 compares structural details of an ion ensemble consisting of 500 $^{138}Ba^+$ ions at $T_{sec}=12$ mK in the pseudopotential approximation [(c),(e), and (g)] and including the micromotion [(a), (b),(d), and (f)].

If the ions are close to the x or y axis, their micromotion is parallel to the corresponding axis. This is shown in (d) for a simulated time which is long enough to reproduce the experimental images, and—just for demonstration—in (f) for an unrealistic, much shorter simulated time where this effect

is more obvious. The ions' motional amplitude is the larger, the further away they are from the trap center (z axis). Image (a) is taken along the x axis, so the center is dominated by ions moving perpendicularly to the image plane without a visible effect. The outer two shells are dominated by ions moving up and down in the image plane, so they appear blurred. However, the relevant radial line of sight for the CCD camera is between the electrodes as shown in (b). Here, the blurring is weaker and homogeneous [compare with image (d)].

In general, the images from simulations including micromotion appear more blurred than those from simulations in the pseudopotential. But due to the limited resolution of our imaging systems, this weak effect is not visible in our CCD images. It is an open question whether a higher resolution imaging system could resolve the micromotion details.

IV. CONCLUSION

In this work, we describe a model for the simulation of cold multispecies ion ensembles in linear Paul traps. Newton's equations of motion for all trapped ions were solved for the exact rf trap potential as well as in the pseudopotential approximation. Studies of the influence of rf micromotion on the simulated (long time exposure) images of ion crystals and rf heating effects showed that micromotion is of little importance for ion crystals at secular temperatures below 100 mK. Here, simulations in the pseudopotential approximation with their much shorter computing times can be used to reproduce and interpret experimental data. Various heating effects (including to some extent rf heating) can be modeled by implementing additional velocity kicks with appropriate magnitudes and frequencies. We showed several applications of our simulation model.

It can be used to extract temperatures and numbers of laser-cooled and sympathetically cooled ions from experimental CCD images of ion crystals. It also allows detailed studies of the sympathetic cooling process which helps to understand and improve our experimental work. Furthermore, simulations of radial secular excitation spectra help to identify trapped ion species. One of the open questions to be addressed in future studies is whether the secular excitation method can also lead to a determination of ion numbers of species located entirely outside the laser-cooled ensemble. Such a method, having the advantage of being nondestructive, would be of considerable practical importance.

ACKNOWLEDGMENTS

We thank H. Wenz and J. Koelemeij for helpful discussions. We gratefully acknowledge funding from the EC network HPRN-CT-2002-00290 "Cold Molecules," the DFG, and the Studienstiftung des Deutschen Volkes.

[1] D. J. Larson, J. C. Bergquist, J. J. Bollinger, W. M. Itano, and D. J. Wineland, Phys. Rev. Lett. **57**, 70 (1986).
[2] M. D. Barrett *et al.*, Phys. Rev. A **68**, 042302 (2003).
[3] B. Roth *et al.*, J. Phys. B **38**, 3673 (2005).
[4] A. Ostendorf *et al.*, Phys. Rev. Lett. **97**, 243005 (2006).
[5] K. Mølhave and M. Drewsen, Phys. Rev. A **62**, 011401 (2000).
[6] T. Baba and I. Waki, J. Chem. Phys. **116**, 1858 (2002).
[7] P. Blythe *et al.*, Phys. Rev. Lett. **95**, 183002 (2005).
[8] B. Roth *et al.*, Phys. Rev. A **73**, 042712 (2006).
[9] P. O. Schmidt *et al.*, Science **309**, 749 (2005).
[10] J. Koelemeij *et al.*, Phys. Rev. Lett. **98**, 173002 (2007).
[11] J. M. Haile, *Molecular Dynamics: Elementary Methods* (John Wiley and Sons, New York, 1997).
[12] M. P. Allen and D. J. Tildesley, *Computer Simulation of Liquids* (Clarendon Press, Oxford, 1987).
[13] A. Rahman and J. P. Schiffer, Phys. Rev. Lett. **57**, 1133 (1986).
[14] J. P. Schiffer, Phys. Rev. Lett. **61**, 1843 (1988).
[15] V. L. Ryjkov, X. Z. Zhao, and H. A. Schuessler, Phys. Rev. A **71**, 033414 (2005).
[16] L. Hornekær, Ph.D. thesis, University of Århus, 2000.
[17] S. Schiller and C. Lämmerzahl, Phys. Rev. A **68**, 053406 (2003).
[18] M. Bussmann *et al.*, Int. J. Mass. Spectrom. **251**, 179 (2005).
[19] B. Roth, P. Blythe, and S. Schiller, Phys. Rev. A **75**, 023402 (2007).
[20] M. J. Jensen, T. Hasegawa, J. J. Bollinger, and D. H. E. Dubin, Phys. Rev. Lett. **94**, 025001 (2005).
[21] In fact, the stochastic force $\boldsymbol{F}_i^{\text{stochastic}}$ is implemented by the velocity kick model (see Sec. II B).
[22] P. K. Gosh, *Ion Traps* (Clarendon Press, Oxford, 1995).
[23] R. P. Feynman, *The Feynman Lectures on Physics, Vol. 1* (Prentice Hall, Englewood Cliffs, NJ, 1963).
[24] One can introduce an equivalent micromotion "temperature" $T_{\text{micro}}=E_{\text{tot}}/k_B$. Note the numerical factor of unity since micromotion occurs in two dimensions.
[25] D. J. Berkeland *et al.*, J. Appl. Phys. **83**, 5025 (1998).
[26] R. Blümel, C. Kappler, W. Quint, and H. Walther, Phys. Rev. A **40**, 808 (1989).
[27] J. Prestage *et al.*, Phys. Rev. Lett. **66**, 2964 (1991).
[28] U. Fröhlich, B. Roth, and S. Schiller, Phys. Plasmas **12**, 073506 (2005).
[29] P. Banks, Planet. Space Sci. **14**, 1105 (1966).
[30] D. J. Wineland *et al.*, J. Res. Natl. Inst. Stand. Technol. **103**, 259 (1998).
[31] If the ion velocities and the velocity kicks are correlated, heating or cooling are possible. For example, in the case of collisions with particles of mass m_n at rest, an approximation for buffer gas cooling using cold He gas, the kinetic energy change per ion and collision is $(1/2)m_l\{(m_l^2+m_n^2)/[(m_n+m_l)]^2-1\}v_k^2$ [32]. The kinetic energy rate of change is therefore $dE_l/dt=-2(m_l m_n)/(m_l+m_n)^2\gamma_{\text{elastic}}E_l$, consistent with Eq. (9).
[32] F. G. Major and H. G. Dehmelt, Phys. Rev. **170**, 91 (1968).
[33] J. P. Schiffer, J. Phys. B **36**, 511 (2003).
[34] C. Raab *et al.*, Phys. Rev. Lett. **85**, 538 (2000).
[35] P. Bushev *et al.*, Phys. Rev. Lett. **92**, 223602 (2004).
[36] J. B. Fenn *et al.*, Science **246**, 4926 (1989).
[37] K. Okada *et al.*, Jpn. J. Appl. Phys., Part 1 **45**, 951 (2006).